Novel Lewis Acid-Base Interactions in Polymer-Derived Sodium-Doped Amorphous Si–B–N Ceramic: Towards Main-Group-Mediated Hydrogen Activation

Shotaro Tada, Motoharu Terashima, Daisuke Shimizu, Norifumi Asakuma, Sawao Honda, Ravi Kumar, Samuel Bernard, Yuji Iwamoto

Novel Lewis Acid-Base Interactions in Polymer-Derived Sodium-Doped Amorphous Si-B-N Ceramic: Towards Main-Group-Mediated Hydrogen Activation

Shotaro Tada,[a, b] Motoharu Terashima,[a] Daisuke Shimizu,[a] Norifumi Asakuma,[a] Sawao Honda,[a] Ravi Kumar,[c] Samuel Bernard,[d] and Yuji Iwamoto*[a]

[a] Dr. S. Tada, M. Terashima, D. Shimizu, N. Asakuma, Dr. S. Honda, Dr. Y. Iwamoto
Department of Life Science and Applied Chemistry, Graduate School of Engineering, Nagoya Institute of Technology, Gokiso-cho, Showa-ku, Nagoya 466-8555, Japan
E-mail: iwamoto.yuji@nitech.ac.jp
[b] Dr. S. Tada
Department of Metallurgical and Materials Engineering, Indian Institute of Technology Madras (IIT Madras), Chennai 600036, India
[c] Dr. R. Kumar
Laboratory for High Performance Ceramics, Department of Metallurgical and Materials Engineering, Indian Institute of Technology Madras (IIT Madras), Chennai 600036, India
[d] Dr. S. Bernard
University of Limoges, CNRS, IRCER, UMR 7315, F-87000, Limoges, France

Abstract: Interest is growing in transition metal-free compounds for small molecule activation and catalysis. We discuss the opportunities arising from synthesizing sodium-doped amorphous silicon-boron-nitride (Na-doped a-SiBN). Na^+ cations and 3-fold coordinated B^{III} moieties were incorporated into an amorphous silicon nitride network via chemical modification of a polysilazane followed by pyrolysis in ammonia (NH_3) at 1000 °C. Emphasis is placed on the mechanisms of hydrogen (H_2) activation within Na-doped a-SiBN structure. This material design approach allows the homogeneous distribution of Na^+ and B^{III} moieties surrounded by SiN_4 units contributing to the transformation of the B^{III} moieties into 4-fold coordinated geometry upon encountering H_2, potentially serving as frustrated Lewis acid (FLA) sites. Exposure to H_2 induced formation of frustrated Lewis base (FLB) N^-= sites with Na^+ as a charge-compensating cation, resulting in the in situ formation of a frustrated Lewis pair (FLP) motif ($\equiv B^{FLA}\cdots H^{\delta-}\cdots H^{\delta+}\cdots :N^-(Na^+)=$). Reversible H_2 adsorption-desorption behavior with high activation energy for H_2 desorption (124 kJ mol^{-1}) suggested the H_2 chemisorption on Na-doped a-SiBN. These findings highlight a future landscape full of possibilities within our reach, where we anticipate main-group-mediated small molecule activation will have an important impact on the design of more efficient catalytic processes and the discovery of new catalytic transformations.

Introduction

Heterogeneous catalysts have been recognized for their potential in activating small molecules such as H_2, CO_2, and N_2 for valuable products. While transition metals (TM) have traditionally been used as catalysts due to their electronic and coordination flexibility, recent interest has grown in main-group elements as catalysts,[1] driven by the need for earth-abundant and cost-effective alternatives. Introducing the frustrated Lewis pair (FLP) concept in the mid-2000s marked a turning point for main-group-mediated small molecule activation.[2] FLP is a simple combination of Lewis acids (LA) such as boron (B)/aluminum (Al) and bases (LB) such as phosphorus (P)/nitrogen (N), but with steric hindrance to prevent the irreversible formation of classical Lewis pair (CLP). [3] Like traditional catalysts, molecular-based homogeneous FLPs are investigated for the activation of small molecules and C–H bonds.[4] Small molecule activation has important applications in biology, medicine, and energy-related fields such as using CO_2 as a C1 building block in organic synthesis.[5] The process must meet specific requirements to achieve desired outcomes, such as altering reaction pathways, enhancing reactivity and selectivity, and enable new processes and reactions that are thermodynamically and kinetically unfavorable in the ground state of the substrate. FLPs have the potential to offer enhanced reactivity and selectivity through bi- or multi-functional site systems, distinguishing them from single-site-based catalysts.[6] Therefore, it is crucial to develop FLPs for extending their application to novel processes while developing new reactions. Moreover, the FLP concept has been recently extended to solid-state systems[7] including oxide systems (γ-Al_2O_3[8] AlOOH[9] $In_2O_{3-x}(OH)_y$[10] and CeO_2[11]) and non-oxide systems, e.g., hexagonal boron nitride (h-BN).[12] Recent studies on bifunctional acid-base reactions in direct catalytic CO_2 hydrogenation to formic acid highlight the potential of FLPs, [13] urging more systematic exploration in sustainable chemical synthesis. These advances underscore the potential of FLPs in crucial processes like CO_2 hydrogenation and ammonia synthesis, paving the way for new approaches in sustainable chemistry.

The BN-based solid-state FLP has been indeed reported with defect-regulated h-BN, where active sites exist between unsaturated (*i.e.*, 2-fold coordinated or fewer) B and N.[12] Therefore, the number of active sites is controlled via defect regulation, making precise reactivity tuning and stability control difficult. In contrast, molecular-based homogeneous FLP

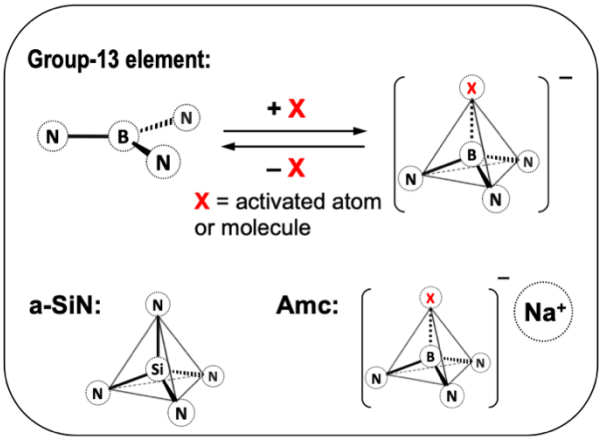

Figure 1. Molecular components in Na-doped amorphous SiBN as main-group mediated small molecule activation catalysts.

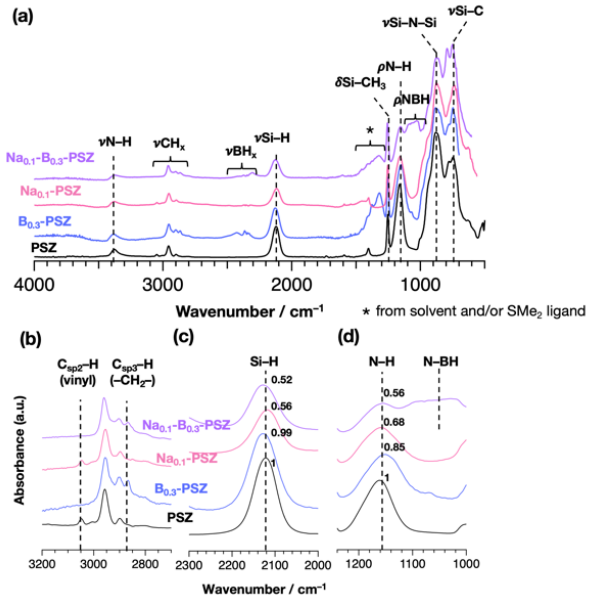

Figure 2. ATR-FTIR spectra of PSZ and as-derived precursors: (a) full-scale ATR-FTIR spectra and the enlarged spectra in the range between (b) 3200-2700, (c) 2300-2000 and (d) 1240-1000 cm^{-1}.

catalysts initially exhibit a neutral coordination state (*e.g.,* 3-fold coordinated for B and N), and form a zwitterionic structure upon activation of small molecules.[4] Reactivity can be easily tuned by adjusting the ligands. Thus, it is noteworthy that there is a clear structural gap between heterogeneous defect-regulated FLPs and molecular-based homogeneous FLPs.

Herein, we tackle the challenge of extending the concept of the molecular-based FLPs to solid-state systems by exploiting the chemical flexibility of preceramic polymers, among them the family of organosilicon polymers,[14] which are involved in the design of Polymer-Derived Ceramics (PDC). The thermochemical conversion of an N-donor organosilicon polymer—namely polysilazane (as a Lewis base)—into an amorphous silicon nitride (a-SiN) scaffold indeed allowed for flexible pore size control, which function as nanoconfined reaction fields. The chemical modification of this polysilazane by boron (B), a naturally abundant and low-toxicity Lewis acid (LA) center, and sodium (Na) for charge compensation before its thermochemical conversion in flowing ammonia (NH_3) delivered alkali metal cation (Amc)-doped amorphous SiBN (Na-doped SiBN) as main-group mediated small molecule activation catalysts (Figure 1).

In detail, controlled contents of B (using borane dimethylsulfide ($BH_3{\cdot}SMe_2$) complex) and Na (using sodium hydride (NaH)) are introduced at molecular scale in a polysilazane (Durazane®1800, labeled PSZ) followed by heat treatment of the as-obtained polymer labeled **Na_x-B_y-PSZ**—where the Na/Si and B/Si molar ratios are tailored (x = 0 or 0.1, y = 0 or 0.3)—in flowing ammonia (NH_3) at 1000 °C. In the delivered Na-doped a-SiBN compound labeled **Na_x-SiB_yN** (x = 0 or 0.1, y = 0 or 0.3), the 4-fold coordinated SiN_4 unit can serve as a structural motif for the transformation of the as-formed 3-fold coordinated BN_3 (B^{III}) units into 4-fold coordinated $[BN_3X]^-$ (B^{IV}) units (X is an activated small molecule) with the contribution of Na to enhance this transformation. We also hypothesized that Amc boosts the basicity of nitrogen atoms within the a-SiN matrix, inspired by compounds like lithium diisopropylamide acting as an sp^3 deprotonation reagent.[15] The potential impact of this work is demonstrated in activating H_2. Thus, we applied ex situ and in situ spectroscopic techniques, including solid-state magic angle spinning nuclear magnetic resonance (MAS-NMR) and temperature-programmed desorption (TPD) to examine the properties of Na-doped a-SiBN and the dynamic shifts of FLP sites when exposed to H_2. Remarkable H_2 adsorption and desorption behaviors are demonstrated. Below are our major highlights.

Results and Discussion

Synthesis and characterization of Na-doped a-SiBN

Central to our process is the commercially available polysilazane Durazane®1800, which is used as a preformed polymer with reactive units such as vinyl groups and Si–H and N–H bonds, to offer a platform for the introduction of B and Na at molecular scale. Attenuated total reflection Fourier transform infrared (ATR-FTIR) spectroscopy of the evolutive precursor from PSZ to **$Na_{0.1}$-$B_{0.3}$-PSZ** (Figure 2) confirms the incorporation of these elements. The reference FTIR spectrum of as-received PSZ was first recorded and confirmed the appearance of bands (ATR, cm^{-1}) at 3379 (br) (νN–H), 3048 (w) (νC_{sp2}–H), 2957 (m) (νC_{sp3}–H), 2121 (s, br) (νSi–H), 1590 (w) (νC=C), 1404 (w) (δC–H, vinyl), 1254 (s) ($\delta Si–CH_3$), 1160 (s, br) (ρSi_2N–H), 881 (vs, br) (νSi–N–Si), and 746 (vs, br) (νSi–C) cm^{-1}.[16] The signal intensity was normalized to the νSi–N–Si band centered at 881 cm^{-1} to compare the ATR-FTIR spectra for as-synthesized samples.

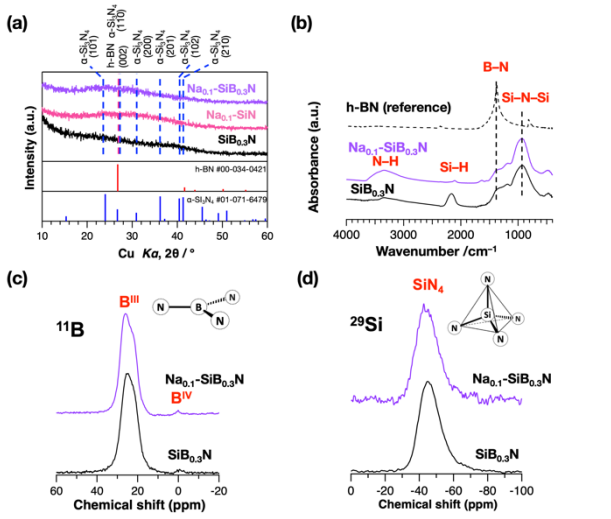

Figure 3. (a) PXRD patterns of $Na_{0.1}$-$SiB_{0.3}N$, $Na_{0.1}$-SiN and $SiB_{0.3}N$ samples; (b) FTIR spectra of as-pyrolyzed samples; (c) ^{11}B and (d) ^{29}Si solid-state NMR spectra of $Na_{0.1}$-$SiB_{0.3}N$ and $SiB_{0.3}N$ samples.

The ATR-FTIR spectrum of the boron-modified sample labeled **$B_{0.3}$-PSZ** (Figure 2b) exhibits a decrease in the relative intensity of C_{sp2}–H band at 3048 cm^{-1} in vinyl groups and the formation of the C_{sp3}–H band (–CH_2–, 2867 cm^{-1}). This suggests the formation of carboborosilane units (≡Si–CH_2–CH_2–B=/≡Si–CH(B=)–CH_3) through a hydroboration reaction between PSZ and BH_3·SMe_2.[16b] In the **$B_{0.3}$-PSZ** sample, while the relative intensity (0.99) of Si–H band at 2120 cm^{-1} remained unchanged (Figure 2c) compared to the initial intensity of Si–H observed in the spectrum of PSZ, the band at 1160 cm^{-1} assigned to N–H bonds showed a slight decrease in the relative intensity (0.85) with a shift to a lower wavenumber (Figure 2d). This suggests the occurrence of dehydrocoupling reaction of N–H/B–H. The shift is attributed to the overlap with remaining BH_3 deformation peaks,[17] where the BH_3 stretching vibration is still observed at 2280–2550 cm^{-1} (Figure 2a). Therefore, these results suggest that when we solely modify the PSZ with BH_3·SMe_2, the hydroboration and dehydrocoupling reaction of N–H/B–H dominate, and hydrosilylation and dehydrocoupling reaction of N–H/Si–H might be minor under the present reaction conditions (0°C for 1 h, and R.T. for 24 h). In the **$Na_{0.1}$-PSZ** and **$Na_{0.1}B_{0.3}$-PSZ** samples, a substantial decrease in the relative intensity of the Si–H and N–H bands is observed (Figures 2c and 2d). In addition, the BH_3 stretching vibration peaks at 2280–2250 cm^{-1} decreased compared to **$B_{0.3}$-PSZ**. Furthermore, a new band can be observed in the spectrum of the **$Na_{0.1}B_{0.3}$-PSZ** sample at 1020–1100 cm^{-1}, assigned to the NBH deformation vibrational mode,[17] suggesting preferential dehydrocoupling reactions between Si–H/N–H and B–H/N–H in Na-modified samples. To understand in detail the role of Na^+, we have investigated ^{23}Na NMR spectroscopy. The associated spectrum of the **$Na_{0.1}$-$B_{0.3}$-PSZ** sample (Figure S1) shows a broad signal centered at –8.6 ppm, which is solely fitted by a single sub-peak as Peak 1 at -8.6 ppm, corresponding to the Na^+ cation.[18] The area fraction of Peak 2 around 19 ppm which may be due to the residual NaH species[19] is less than 1 %; thus, it has been omitted. Therefore, it is obvious that a reaction between PSZ and NaH occurs and we propose that Na^+ cation formed a possible complex with PSZ, *e.g.*, sodium silylamide complex (≡Si–N^-(Na^+)–Si≡). This alkali amide formation could initiate the potential dehydrogenative coupling reactions. Based on the literature[20], two possible reaction pathways mediated by alkali amide compounds have been suggested, involving hypervalent silicate intermediates or σ-bond metathesis as shown in Scheme S1. These results indicate that the NaH-catalyzed dehydrocoupling reaction efficiently promotes the formation of the Si–N network and the incorporation of boron species into the Si–N network via B–N bond formation during the precursor synthesis step.

The **Na_x-B_y-PSZ** samples are then pyrolyzed under NH_3 at 1000 °C for 2 h to afford the compounds labeled **Na_x-SiB_yN** (x = 0 or 0.1, y = 0 or 0.3). Characterization results mainly gained from these samples are compared with results obtained from **$SiB_{0.3}N$**, **$Na_{0.1}$-SiN** and **$Na_{0.1}$-$SiB_{0.3}N$** obtained in the same pyrolysis conditions from **$B_{0.3}$-PSZ** and/or **$Na_{0.1}$-PSZ**, and **$Na_{0.1}$-$B_{0.3}$-PSZ** respectively. The powder X-ray diffraction (PXRD) pattern of the representative **$Na_{0.1}$-$SiB_{0.3}N$** sample (Figure 3a) (and also **$Na_{0.1}$-SiN**) distinguishes a very diffuse peak from 20 to 40 ° which is not identified in the XRD pattern of **$SiB_{0.3}N$**. This peak can fit with the positions of the peak series corresponding to α-Si_3N_4 (ICDD PDF card #01-071-6479). In addition, it can be envisioned that the restricted 20–30° range in the pattern of **$Na_{0.1}$-$SiB_{0.3}N$** fits with the (002) diffraction peak of sp^2-BN (ICDD PDF card #00-034-0421). To further get structural information on **$Na_{0.1}$-$SiB_{0.3}N$**, its transmission mode FTIR spectrum has been recorded using the conventional KBr disk method (Figure 3b). It shows the bands attributed to the Si–N–Si stretching mode at around 920 cm^{-1} [21] and the B–N in-plane optical phonon mode,[22] at 1350 cm^{-1} as in **$SiB_{0.3}N$**; thereby, confirming the presence of B–N bonds within the a-SiN matrix. Additionally, a distinct broad peak centered around 2200 cm^{-1}, indicative of the Si–H stretching mode, is evident in **$SiB_{0.3}N$** but notably absent in **$Na_{0.1}$-$SiB_{0.3}N$**. The absence of the Si–H stretching mode in **$Na_{0.1}$-$SiB_{0.3}N$** suggests the promotion of dehydrocoupling reactions between Si–H/N–H and B–H/N–H pairs facilitated by the NaH modification during the polymer synthesis stage. This observation aligns with an earlier report by Seyferth and Wiseman[23] on dehydrogenative coupling reactions of ammonolysis products of CH_3SiHCl_2, CH_3SiHNH_n (n>3) to afford polyorganosilazanes by using a basic catalyst such as potassium hydride (KH). Therefore, the incorporation of Na into a-SiBN matrix contributes to the partial crystallization of Si_3N_4 or sp^2-BN phase in the short-range order as shown in the XRD patterns. The elemental analysis highlights that the amount of Na in **$Na_{0.1}$-$SiB_{0.3}N$** and **$Na_{0.1}$-SiN** can be controlled by the Na/Si ratio (Na/Si = 0.1) fixed in the early stage of the process; thereby, at the polymer synthesis stage (Table S1 and Figure S2). It is also shown that the carbon content is low, and oxygen content is slightly higher in the Na-doped **$Na_{0.1}$-$SiB_{0.3}N$** and **$Na_{0.1}$-SiN** samples than in **$SiB_{0.3}N$** (Table S1). These results are primarily due to the catalytic effect of Na^+ similar to Scheme S1 which promotes the formation of Si–N or B–N bonds during pyrolysis in flowing NH_3. In addition, it is also suggested that the as-formed Si–C and B–C bonds are effectively converted into Si–N and B–N under NH_3 in the presence of Na^+ through bond cleavage and redistribution reactions. Furthermore, in the FTIR spectra (Figure 3b) **$Na_{0.1}$-$SiB_{0.3}N$** sample displays a relatively large and broad peak around 3400 cm^{-1}, attributed to hydrogen-bonded N–H groups, suggesting that oxygen incorporation is a secondary result of hydrogen bond formation between surface N–H groups and H_2O. Na^+ cations are uniformly distributed within the a-SiN matrix as revealed by EDS mapping analysis (Figure S3). To definitively conclude the presence of B–N in the **$Na_{0.1}$-$SiB_{0.3}N**

sample, its ^{11}B MAS-NMR spectrum (Figure 3c) shows signals corresponding to 3-fold coordinated B^{III} units at 15–35 ppm[24] and 4-fold coordinated B^{IV} units at 0 ppm[25] as for the **$SiB_{0.3}N$** sample. The ^{29}Si CP MAS-NMR spectra (Figure 3d) exhibit a broad signal at –44.5 ppm, corresponding to the SiN_4 units in the amorphous SiN matrix [26] and corroborates FTIR observations. The ^{23}Na MAS-NMR spectrum (Figure S4) confirmed the presence of the charge-compensating Na^+ cation. [18, 27] These results reveal the successful incorporation of Na^+ and B^{III} units within the a-SiN matrix; thus, validating the synthesis strategy.

Lewis acid-base property of polymer-derived Na-doped a-SiBN

Theoretical studies on FLPs reported that the effective spatial distance between the active centers of reactive FLPs falls within the microporous region.[28] Therefore, the porosity of $Na_{0.1}$-$SiB_{0.3}N$ and $Na_{0.1}$-SiN samples at the mesoscopic length scale was characterized by N_2 adsorption and desorption measurement at –196 °C (Figures 4a and b) before investigating their acid-base properties (Figures 4c and d). The micro- and meso-pores produced during the conversion of polysilazane to Si-based non-oxide ceramics are generally unstable and tend to collapse above 800 °C under flowing NH_3. [29] Therefore, it is acceptable that the **$SiB_{0.3}N$** sample exhibits type III isotherms, suggesting a non-porous structure (Figure 4a). In contrast, the N_2 adsorption and desorption isotherms (Figure 4a) and the pore size distribution (PSD) curves (Figures 4b and Figure S5) indicate that the **$Na_{0.1}$-$SiB_{0.3}N$** sample exhibits micro-/meso-porous nature (Type I+IV according to the IUPAC classification[30]) with the most distinct uptake at $p/p_0 < 0.1$ associated with the filling of micropores. The hysteresis loop observed at $p/p_0 > 0.5$ confirms the presence of mesopores. In contrast, the **$Na_{0.1}$-SiN** sample shows Type I isotherms with micro-pores being the dominant feature. The microporosity detected in the **$Na_{0.1}$-$SiB_{0.3}N$** and **$Na_{0.1}$-SiN** is expected to offer an effective nanospace accessible to H_2 activation. Measurements were also conducted on a microporous **a-SiN** sample to evaluate the acid-base property of Na- and B-free sample. Our previous study[31] found that the chemical modification of PSZ with $InCl_3$ would result in the formation of micropores that are stable at high temperatures during pyrolysis under ammonia up to 1000 °C, while the In species were thought to decompose to be removed completely as volatile species. In the present study, we have used this material as a homemade microporous **a-SiN** (*see ESI for the synthetic details*). The **a-SiN** sample displays a type I+IV behavior in the N_2 adsorption-desorption isotherms (Figure 4a and more detailed in Figure S6). The Brunauer–Emmett–Teller (BET) surface areas and pore volumes are summarized in Table S2. The resulting BET surface area of the **$Na_{0.1}$-$SiB_{0.3}N$**, **$Na_{0.1}$-SiN, $SiB_{0.3}N$**, and **a-SiN** samples were measured to be 263, 244, 27 and 285 $m^2\ g^{-1}$, respectively. The total pore volume ($V_{BET,\ total}$) of **$Na_{0.1}$-$SiB_{0.3}N$**, **$Na_{0.1}$-SiN, $SiB_{0.3}N$**, and **a-SiN** samples were measured to be 0.17, 0.21, 0.05 and 0.20 $cm^3\ g^{-1}$, respectively. The micropore volumes (V_{micro}) of **$Na_{0.1}$-$SiB_{0.3}N$**, **$Na_{0.1}$-SiN,** and **a-SiN** samples were measured as 0.13 0.11, and 0.12 $cm^3\ g^{-1}$, respectively. Thus, the micropore

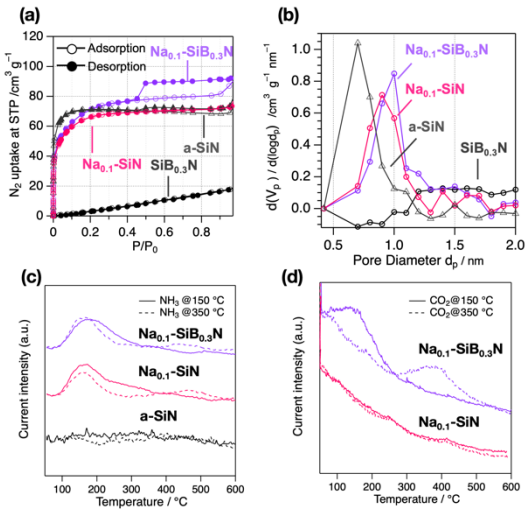

Figure 4. (a) N_2 adsorption and desorption isotherms at –196 °C for Na_x-SiB_yN (x = 0 or 0.1, y = 0 or 0.3) samples and reference a-SiN sample[31], the open and filled marks represent N_2 adsorption and desorption isotherm, respectively; the resulting pore size distribution (PSD) curves characterized by the (b) MP plot; (c) NH_3-TPD-MS spectra under flowing He; (d) CO_2-TPD-MS spectra under flowing He.

volume was almost constant values for the microporous samples in this study.

The formation of micro-/meso-pore observed in the Na-doped samples is similar to previously investigated materials where in situ generation of hydrogen from the thermal decomposition of NH_3 facilitated the creation of stable micro-/meso-pores.[32] We suggest that the B–N and Si–N bonds formed via NaH-catalyzed dehydrocoupling reactions followed by the pyrolysis under NH_3 exhibit reactivity with the in situ formed H_2 at elevated temperatures. As a result, these sites can be repeatedly cleaved and recombined through the reaction, leading to the formation of H_2-accessible active pores. The formation of mesopores in the **$Na_{0.1}$-$SiB_{0.3}N$** sample can be attributed to the lower coordination number of incorporated B(III) compared to Si (IV). This difference facilitates the formation and growth of larger pore clusters via the percolation mechanism during the repeated bond cleavage and recombination, leading to the observed mesopores.

The acid-base properties of **$Na_{0.1}$-$SiB_{0.3}N$** (S_{BET} = 263 $m^2\ g^{-1}$) and **$Na_{0.1}$-SiN** (S_{BET} = 244 $m^2\ g^{-1}$), and **a-SiN** (S_{BET} = 285 $m^2\ g^{-1}$) samples have been explored using probe molecules by in situ spectroscopic analysis. Figure 4c and Figure 4d give an overview of the resulting acid-base properties determined by NH_3- and carbon dioxide (CO_2)-TPD measurements coupled with mass spectrometry (TPD-MS). Notably, the Na-free **$SiB_{0.3}N$** sample is nonporous (Figure 4a), and no NH_3 and CO_2-TPD peaks were observed (Figure S7). This is due to the low activity of the incorporated B^{III} sites or limited access of the probe molecules to the reactive sites. NH_3-TPD-MS profiles recorded after NH_3 exposure at 150 °C (Figure 4c) indicate a broad peak around 200 °C for the **$Na_{0.1}$-$SiB_{0.3}N$** and **$Na_{0.1}$-SiN** samples. On the other hand, no peak is observed on **a-SiN** sample. This clearly indicates that Na-cation doping contributes to the formation of acid sites. Deconvolution of the NH_3-TPD-MS profiles for the **$Na_{0.1}$-$SiB_{0.3}N$** and **$Na_{0.1}$-SiN** samples (Figure S8) results in four sub-peaks. The first peak (Peak 1) centered at 157 °C in both samples originates

from the desorption of NH_3 from a weak acid site associated with the Na^+ cation. [33] Peaks 2–4 appear at different temperatures, with variations in the local structural environment of the acidic sites between the **$Na_{0.1}$-$SiB_{0.3}N$** and **$Na_{0.1}$-SiN** samples. The normalized NH_3-TPD-MS profile of the **$Na_{0.1}$-$SiB_{0.3}N$** sample recorded after NH_3 exposure at 350 °C shows a decrease in the signal corresponding to Peak 2, and a new peak appeared at around 450 °C. This shift indicates that weakly adsorbed NH_3 transitions to a more strongly adsorbed state, signifying the existence of Lewis acid sites.

The CO_2-TPD-MS profiles (Figure 4d) reveal a pronounced CO_2 desorption behavior for the **$Na_{0.1}$-$SiB_{0.3}N$** sample, with a peak observed around 150 °C after CO_2 exposure at 150 °C. And following CO_2 exposure at 350 °C, the peak shifts to a higher temperature of 380 °C. In contrast, the **$Na_{0.1}$-SiN** sample exhibits a limited ability to adsorb CO_2. CO_2 is known to interact with basic sites[34] and can also interact with FLP sites.[10, 35] The polymer-derived **$Na_{0.1}$-$SiB_{0.3}N$** sample consists mainly of an amorphous network with micropores below 1.5 nm in size (Figure 4b). The FLP sites investigated in this study were formed in situ within the microporous **$Na_{0.1}$-$SiB_{0.3}N$** network. When pre-exposure to CO_2 at 350 ºC, the CO_2 molecules could be sufficiently activated to permeate through the microporous amorphous **$Na_{0.1}$-$SiB_{0.3}N$** matrix to reach the FLP sites. Based on this assumption, it is strongly suggested that the broad CO_2-TPD-MS peak around 150 ºC after exposure to CO_2 at 150 ºC is assigned to CO_2 physisorption, primarily associated with the weak basic sites on the sample surface. In contrast, the broad peak centered at 380 ºC after exposure to CO_2 at 350 °C is attributed to the strong acid-base sites, i.e. the FLP sites formed in situ within the microporous amorphous **$Na_{0.1}$-$SiB_{0.3}N$** matrix. These findings suggest that the **$Na_{0.1}$-$SiB_{0.3}N$** sample possesses both Lewis acid and base pair sites, facilitating NH_3 adsorption (Lewis acid sites) and CO_2 adsorption (Lewis acid-base pair sites) and contributing to its enhanced NH_3 and CO_2 affinity.

Hydrogen adsorption and desorption properties of polymer-derived Na-doped a-SiBN and those mechanistic investigations

The reversible hydrogen splitting of the **Na_x-SiB_yN** samples (x = 0 or 0.1, y = 0 or 0.3) is further studied by H_2-TPD measurements. Before monitoring the H_2-TPD profiles, the samples are maintained at 650 °C under flowing Ar and subsequently exposed to H_2 at specific temperatures (T_{H2} = 150, 250, 350, and 450 °C). The H_2-TPD profiles of the **$SiB_{0.3}N$** sample (x = 0, y = 0.3) (Figure 5a) show no detectable peaks, indicating the absence of H_2 desorption. In contrast, the H_2-TPD profiles of the **$Na_{0.1}$-$SiB_{0.3}N$** sample (x = 0.1, y = 0.3) (Figure 5b) exhibit broad peaks at each T_{H2}, with increasing intensity and position as T_{H2} increases. Similar behavior is observed in the H_2-TPD profiles of the **$Na_{0.1}$-SiN** sample (x = 0.1, y = 0) (Figure S9a), while the microporous **a-SiN** sample (x = 0, y = 0) has no distinct peaks (Figure S9b). These results are clearly attributed to both microporosity and the incorporation of Na sites at the molecular scale. The cyclic behavior of hydrogen adsorption and desorption is investigated on the **$Na_{0.1}$-$SiB_{0.3}N$** sample through 10 consecutive H_2-TPD measurements at T_{H2} = 350 °C (Figure 5c). The cyclic H_2-TPD spectra demonstrate declining intensity for the

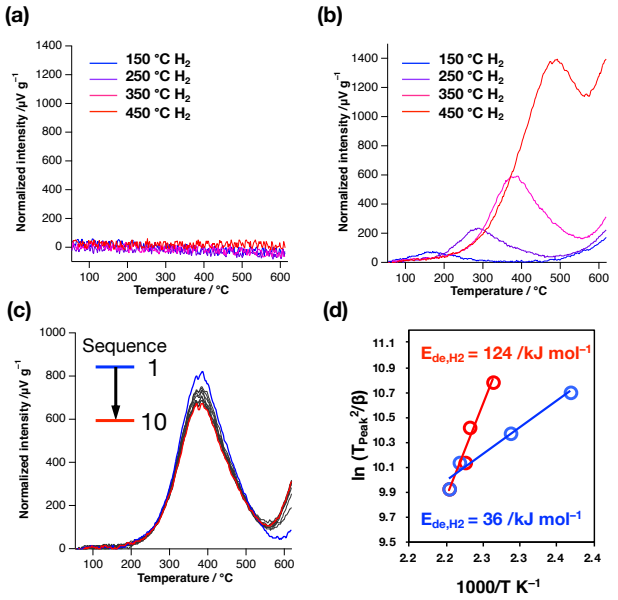

Figure 5. H_2-TPD profiles for Na_x-SiB_yN (x = 0 or 0.1, y = 0 or 0.3) samples at specific H_2-exposure temperatures (T_{H2}) of 150, 250, 350, and 450 °C: (a) $SiB_{0.3}N$ and (b) $Na_{0.1}$-$SiB_{0.3}N$ samples; (c) Cyclic H_2-TPD measurement at T_{H2} of 350 °C up to 10 cycles for $Na_{0.1}$-$SiB_{0.3}N$; and (d) Plot of $\ln(T_p^2/\beta)$ vs. $1000/T_p$, where β is the temperature ramping rate and T_p is the absolute peak temperature. The activation energy for H_2 desorption at T_{H2} of 150 °C was estimated from the slope of the straight line for $Na_{0.1}$-$SiB_{0.3}N$ (red, 124 kJ mol^{-1}) and $Na_{0.1}$-SiN (blue, 36 kJ mol^{-1}) samples.

dominant peak, centered at 390 °C, over the first 7 cycles, eventually reaching a saturation intensity by the 10th cycle. An emergent shoulder peak above 600 °C during the cyclic measurements also reaches consistent intensity after 10 cycles.

The N_2 adsorption/desorption measurement at –196 °C before and after the cyclic TPD measurements (Figure S10a) indicates slight changes in their isotherms whereas the PSD curves (Figures S10b and c) are hardly changed, confirming the stable micro-/meso-porous nature during the cyclic H_2-Ar treatment at high temperature. The activation energy for H_2 desorption in the **$Na_{0.1}$-$SiB_{0.3}N$** and **$Na_{0.1}$-SiN** samples has been estimated using Redhead analysis.[36] The Arrhenius-type plot of $\ln(T_p^2/\beta)$ versus $1000/T_p$, where β represents the temperature ramping rate and T_p is the absolute peak temperature, yielded straight lines for the H_2-TPD profiles recorded at T_{H2} = 150 °C (Figure 5d). The activation energies for H_2 desorption ($\Delta E_{d,H2}$) are calculated to be 124 kJ mol^{-1} for **$Na_{0.1}$-$SiB_{0.3}N$** and 36 kJ mol^{-1} for **$Na_{0.1}$-SiN**. The distinct difference in the $\Delta E_{d,H2}$ values indicates different adsorption-desorption processes for the two samples, with the **$Na_{0.1}$-$SiB_{0.3}N$** sample exhibiting a stronger interaction with H_2, as evidenced by its higher $\Delta E_{d,H2}$ value. Zhuofeng et al. performed the DFT study of the geometric and electronic effects on the state-of-the-art molecular-based FLPs with intramolecular B~N systems for H_2 activation. [37] The calculated free energy change for hydrogen adsorption products and transition states of ansa-aminoboranes, *ortho*-NMe_2-C_6H_4-$B(C_6F_5)_2$ and, *ortho*-TMP-C_6H_4-BH_2 (TMP = 2,2,6,6-tetra-methylpiperidine), ranges between 75–116 kJ mol^{-1}.[37] In our present study, the $\Delta E_{d,H}$ of the Na-SiBN sample is 124 kJ mol^{-1}. Compared with the state-of-the-art molecular-based

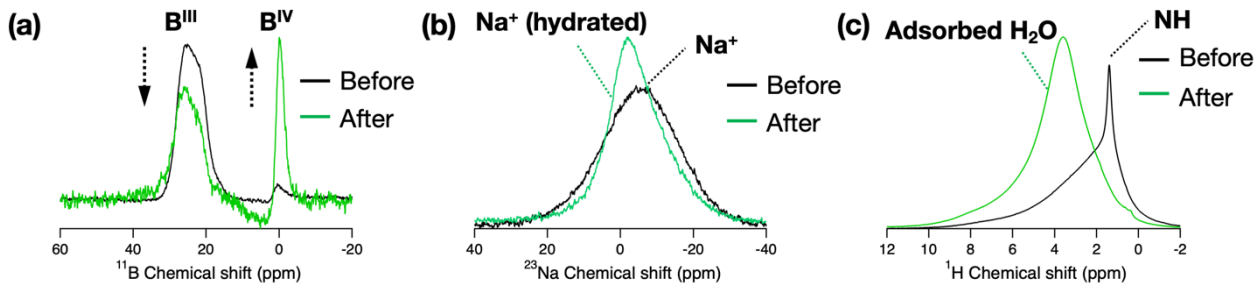

Figure 6. Line shape ss-MAS NMR study for **$Na_{0.1}$-$SiB_{0.3}N$** sample before and after ex situ X-ray irradiation: (a) ^{11}B, (b) ^{23}Na, (c) ^{1}H ss-MAS NMR spectra.

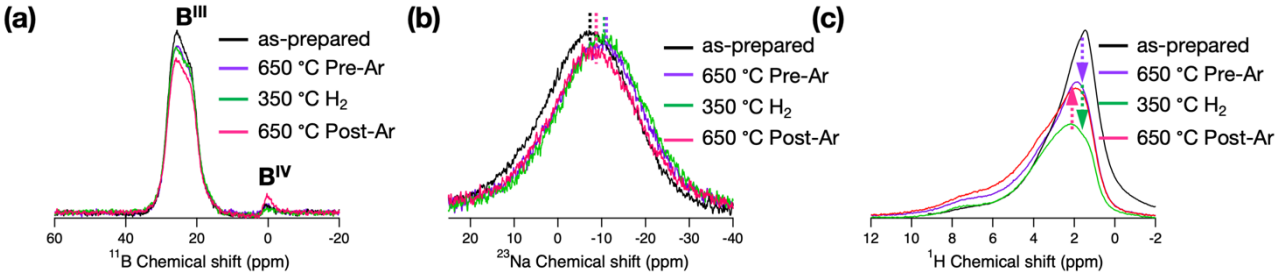

Figure 7. Line shape ss-MAS NMR study for **$Na_{0.1}$-$SiB_{0.3}N$** sample before and after pre-treatment under Ar, ex situ H_2 adsorption at 350 °C and following post-treatment under Ar: (a) ^{11}B, (b) ^{23}Na, (c) ^{1}H ss-MAS NMR spectra

FLPs, this value is within a reasonable range. Based on these results, we investigated the local structure around key nuclei (^{1}H, ^{11}B, ^{23}Na) using ex situ MAS-NMR. The objective was to identify preferential H_2 adsorption sites. Initially, to characterize the functionality of the boron site as a Lewis acid site (as illustrated in Figure 1), we have recorded MAS-NMR spectra before and after X-ray irradiation in air with the target small molecules being H_2O or CO_2. The X-ray irradiation experiment is performed to observe the transition in the coordination number of boron sites (*i.e.*, from III to IV). The MAS-NMR spectra of the **$Na_{0.1}$-$SiB_{0.3}N$** sample exhibit significant changes following X-ray irradiation compared to the initial spectra (Figures 6a–c). In the ^{11}B MAS-NMR spectrum, the relative intensity of B^{IV} units significantly increases after X-ray irradiation (Figure 6a). In contrast, the ^{11}B MAS-NMR signal for the **$SiB_{0.3}N$** sample remains almost unchanged (Figure S11). The ^{23}Na MAS-NMR signal becomes sharper and slightly shifts towards lower magnetic fields after X-ray irradiation (Figure 6b), indicating the formation of Na–H_2O complexes (hydrated Na^+).[38] The ^{1}H MAS-NMR spectrum exhibits a distinct signal at 1.4 ppm corresponding to the N–H band[39] which disappears after the X-ray irradiation. In parallel, a new broad signal appears at 3.7 ppm after the X-ray irradiation, corresponding to the adsorption of H_2O molecules originating from moisture in the air (Figure 6c).[38a] These results confirm that B^{III} units in conjunction with Na^+ surrounded by SiN_4 units lead to the formation of B^{IV} units in the presence of small molecules, serving as preferential adsorption sites for H_2. Further analysis has been conducted to examine the local structural changes before and after H_2 adsorption at 350 °C by recording the MAS-NMR signals at the following stage: the **$Na_{0.1}$-$SiB_{0.3}N$** sample underwent pre-treatment under flowing Ar at 650 °C for 30 min (labeled **$Na_{0.1}$-$SiB_{0.3}N$*pre***), exposure to H_2 at 350 °C for 60 min (labeled **$Na_{0.1}$-$SiB_{0.3}N$*H_2***), and post-treatment under flowing Ar at 650 °C for 30 min (labeled **$Na_{0.1}$-$SiB_{0.3}N$*post***).

The normalized ^{11}B MAS-NMR spectra for the **$Na_{0.1}$-$SiB_{0.3}N$*pre*** and **$Na_{0.1}$-$SiB_{0.3}N$*H_2*** samples (Figure 7a) exhibit a slight decrease in the signal of B^{III} units compared to the as-synthesized **$Na_{0.1}$-$SiB_{0.3}N$** sample, while no change is observed at B^{IV} units. The ^{11}B MAS-NMR signal for the **$Na_{0.1}$-$SiB_{0.3}N$*post*** sample indicates a further decrease in B^{III} units with a slight increase in B^{IV} units, suggesting structural rearrangement during exposure to air. These findings imply that B sites of **$Na_{0.1}$-$SiB_{0.3}N$*pre*** are highly sensitive to the surrounding atmosphere and the presence of probe molecules, indicating that the B centers located within the H_2-accessible micropores are efficiently activated after the pre-treatment. The ^{23}Na MAS-NMR signals (Figure 7b) shift toward higher magnetic fields in the **$Na_{0.1}$-$SiB_{0.3}N$*pre*** and **$Na_{0.1}$-$SiB_{0.3}N$*H_2*** samples, followed by partial recovery to its initial state in the **$Na_{0.1}$-$SiB_{0.3}N$*post*** sample. The change toward a higher magnetic field in the ^{23}Na MAS-NMR signals can be attributed to an increase in the coordination number of Na^+.[19] The lone pair electrons of the N atoms become potential ligands for Na^+ cations, suggesting the formation of Na^+ complex with a-SiN matrix, *i.e.*, Na^+–$(:N\equiv)_n$ complex, during the pretreatment. XPS results for **$Na_{0.1}$-$SiB_{0.3}N$** (and **$Na_{0.1}$-SiN**) indicate a slight broadening of signal toward lower binding energy relative to the **$SiB_{0.3}N$** sample, while the signal positions of other elements (Si *2p*, and B *1s*)

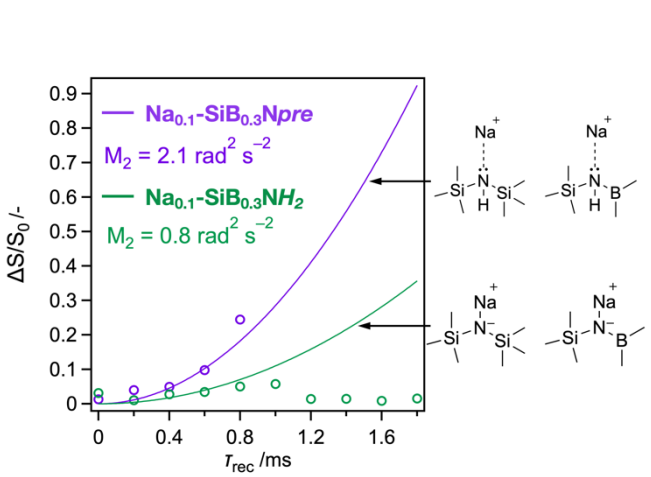

Figure 8. ^{23}Na{^{1}H} REDOR NMR dephasing results ($\Delta S/S_0$) plotted versus dephasing period of τ_{rec} for the $Na_{0.1}$-$SiB_{0.3}$N*pre*, $Na_{0.1}$-$SiB_{0.3}$NH_2, samples.

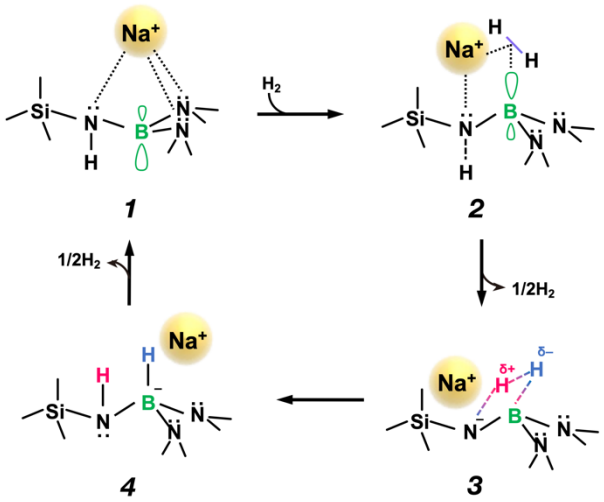

Figure 9. A schematic illustration for the dynamic formation of FLP sites on amorphous Na-containing SiBN and following interaction with H_2.

remain unchanged (Figure S12). A comparable shift to lower binding energy has been observed in Na-doped g-C_3N_4.[40] This is due to the higher electronegativity of N atoms, leading to the formation of a strong interaction with doped Na. Consequently, the electrons of Na could be transferred to N atoms, resulting in the increased electron density of N atoms in **$Na_{0.1}$-$SiB_{0.3}$N** and **$Na_{0.1}$-SiN** samples, which can serve as preferential H_2 adsorption sites as Lewis base sites. ^{1}H MAS-NMR spectra (Figure 7c) reveal the notable reduction in the N–H band at 1.4 ppm for the **$Na_{0.1}$-$SiB_{0.3}$N*pre*** sample. This suggests the desorption of NH_3—which might have been passivated on acidic sites during pyrolysis—occurs during the pre-treatment phase. Upon comparing the spectra from **$Na_{0.1}$-$SiB_{0.3}$N*pre***, **$Na_{0.1}$-$SiB_{0.3}$NH_2**, and **$Na_{0.1}$-$SiB_{0.3}$N*post*** samples, the intensity of the N–H band at 1.4 ppm decreases further following H_2 treatment, then it recovers after post-treatment, approximating the levels observed in the **$Na_{0.1}$-$SiB_{0.3}$N*pre*** sample. It is expected that the exposure of the material to H_2 (**$Na_{0.1}$-$SiB_{0.3}$NH_2**) induces the formation of Na^+ cation complex with H_2[41a,b] *i.e.*, the Na^+–(:N≡)$_{n-x}$(H_2)$_x$ complex. The strength of the interaction of Na^+ cation with coordinated ligands depends on the number of ligands (n)[41b] and the species, therefore, the coordination of Na^+ cation with additional H_2 molecule(s) affects the interaction of Na^+–:N≡ pair. This perturbation promotes subsequent solid-state ion exchange for the formation of Na^+–N^-= moiety, causing a reduction in N–H peak intensity in the ^{1}H MAS-NMR spectra (Figure 7c). It should be noted that the H_2-induced solid-state ion exchange is reversible as the peak intensity of N–H band was almost regained by the post Ar-treatment. The Na^+–N^-= configuration is potentially integral to the FLP site as a Lewis base site that subtracts a proton from a heterolytically dissociated hydrogen molecule.

To delve deeper into the local structural changes before and after H_2 adsorption, we conducted rotational-echo double resonance (REDOR) experiments on the **$Na_{0.1}$-$SiB_{0.3}$N** sample.[42] The REDOR signal decay of pairwise $^{23}Na^+$–H^1(N) dipolar interaction is firstly examined. The Van Vleck dipolar second moment M_2 (^{23}Na–^{1}H) – which reflects the ^{23}Na–^{1}H distance in the structure – is estimated by fitting the signal dephasing ($\Delta S/S_0$) data versus the rotational period (τ_{rec}) up to 0.8 ms (Figure 8). Upon comparing M_2 values before and after H_2 treatment for ^{23}Na–^{1}H pairwise interactions, the M_2 (^{23}Na–^{1}H) data for **$Na_{0.1}$-$SiB_{0.3}$N*pre*** is 2.1 (in 10^6 rad^2 s^{-2}), while that for **$Na_{0.1}$-$SiB_{0.3}$NH_2** is distinctively decreased to 0.8. This indicates that the $^{23}Na^+$–H^1(N) spatial distance is close before hydrogen treatment and opened after hydrogen treatment at 350 °C suggesting that Na^+ cations are initially coordinated with silylamino units (≡Si–N(H)–Si≡) or even with ≡Si–N(H)–B= units to subsequently form Na^+–N^-= after hydrogen treatment. The Na^+–N^-= formation is well consistent with the observed reduction in N–H band in the ^{1}H MAS-NMR spectra (Figure 7c). The REDOR signal decay for the pairwise $^{11}B^{III}$–^{1}H(N) dipolar interaction is also examined. The fitted $\Delta S/S_0$ and extracted M_2 ($^{11}B^{III}$–^{1}H) data for the **$Na_{0.1}$-$SiB_{0.3}$N*pre*, $Na_{0.1}$-$SiB_{0.3}$NH_2** and **$Na_{0.1}$-$SiB_{0.3}$N*post*** samples are shown in Figure S13 and Table S3, respectively. The estimated M_2 ($^{11}B^{III}$–^{1}H) value of 1.80 (in 10^6 rad^2 s^{-2}) for the **$Na_{0.1}$-$SiB_{0.3}$N*pre*** sample decreases to 1.22 for the **$Na_{0.1}$-$SiB_{0.3}$NH_2** sample and recovers to 1.66 for the **$Na_{0.1}$-$SiB_{0.3}$N*post*** sample. These fluctuations suggest dynamic alternations in the spatial distance of the $^{11}B^{III}$–^{1}H(N) pair during H_2 treatment. Specifically, after exposure to H_2, there is a noticeable increase in the distance between ≡B and HN=, indicating the elongation and subsequent dissociation of the NH proton around the ^{11}B nuclei. This supports our hypothesis that H_2 molecules interact with the proposed FLP sites.

Conclusion

Most catalysts rely on critical platinum group metals with limited natural abundance and commonly suffer from drawbacks like coking, restricting continuous large-scale application.

Hence, effective metal-free catalysts could be highly appealing, although such catalysts are less developed. Because the catalytic activities are normally attributed to dopants introduced with various ex situ or in situ processes[43], we explored here the PDC route—and in particular the chemical flexibility of polysilazanes—to design an effective and robust sodium-doped metal-free inorganic compound, namely Na-doped SiBN. Our local structure design at molecular-scale in ceramic materials successfully amplifies the reactivity of B and N sites in the presence of H_2. The

proposed H_2 adsorption and desorption process on the Na-doped a-SiBN ceramic involves several key steps (Figure 9). Initially, B^{III} units and Na^+ sites are successfully incorporated within polysilazanes as a precursor of a microporous a-SiN matrix. N atoms bearing unshared electron pairs are suggested as active ligands for the doped Na^+ cations to form Na^+ complexes, particularly Na^+–$(:N\equiv)_n$. (***1***). This enhances the electron density of N atoms within the a-SiN matrix. Upon accessing the active site within the microporous structure, molecular hydrogen interacts with both the B sites and Na^+ cations, which function as frustrated Lewis acid (FLA) sites (***2***). This is evidenced by ex situ solid-state MAS-NMR measurements, which elucidate the transformation of B^{III} moieties into 4-fold coordinated geometries upon exposure to H_2 at 150 to 450 °C and/or X-ray irradiation at room temperature in presence of H_2O. ^1H MAS-NMR spectra and REDOR experiment revealed that the exposure to H_2 at specific temperatures from 150 to 450 °C also causes elongation and subsequent elimination of N–H proton triggering the formation of FLP sites involving the $\equiv B^{FLA}\cdots H^{\delta-}\cdots H^{\delta+}\cdots :N^-(Na^+)=$ motif (***3***), which contributes to the reversible H_2 adsorption-desorption properties of the Na-doped SiBN ceramic. Eventually, this local structure (***3***) leaves room for the formation of a hydrogen-containing B^{IV} unit with Na^+ acting as a charge-compensating cation, as in (***4***). H_2-TPD measurements confirm the reversible nature of H_2 adsorption and desorption, with a high activation energy for H_2 desorption (124 kJ mol^{-1}) indicative of the chemisorption of H_2 on the FLP sites. Although further investigation is needed to fully understand the dissociation of hydrogen on the Na-doped SiBN surface network, the strong interaction between H_2 molecules and the Na-doped SiBN ceramics is suggested based on molecular orbital interactions within the proposed FLP sites. The amorphous Na-SiBN exhibits much higher thermal stability compared to molecular-based FLPs, making it suitable for catalytic reactions under harsh, high-temperature conditions. This stability offers potential advantages for Na-SiBN as a more convenient and robust catalyst for practical applications. Additionally, PDC can be processed using templates[44] and additive manufacturing technology,[45] enabling the production of ceramic components with tailored shapes and controlled porosity. The NH_3-TPD and CO_2-TPD results indicate significant reactivity with NH_3 and CO2 at high temperatures. These findings underline the potential of Na-SiBN for catalytic applications, particularly in reactions involving CO_2 hydrogenation.[6b] This molecular-based FLP-inspired design approach holds promise for advancing main-group-mediated solid-gas phase interactions in heterogeneous catalysis, thereby offering valuable insights and promising significant impacts in this domain.

Acknowledgments

This research was funded by JSPS KAKENHI, Grant Number JP20K05076, and CNRS via the International Research Project (IRP) 'Functional inorganic materials for global social challenges' labelled FRESH. N. Asakuma acknowledges receiving financial support from JST SPRING, Grant Number JPMJSP2112.

Keywords: polymer-derived ceramics • frustrated Lewis pair • small molecule activation • hydrogen • heterogeneous catalysis

[1] a) P. P. Power, *Nature* **2010**, *463*, 171–177; b) H. Zhou, X. Yi, Y. Hui, L. Wang, W. Chen, Y. Qin, M. Wang, J. Ma, X. Chu, Y. Wang, X. Hong, Z. Chen, X. Meng, H. Wang, Q. Zhu, L. Song, A. Zheng, F. S. Xiao, *Science* **2021**, *372*, 76–80; c) W. Chen, J. Han, Y. Wei, A. Zheng, *Angew. Chemie - Int. Ed.* **2022**, *61*, 1–7.

[2] a) G. C. Welch, R. R. S. Juan, J. D. Masuda, D. W. Stephan, *Science.* **2006**, *314*, 1124–1126; b) D. W. Stephan, G. Erker, *Angew. Chemie - Int. Ed.* **2015**, *54*, 6400–6441.

[3] D. W. Stephan, *Chem* **2020**, *6*, 1520–1526.

[4] D. W. Stephan, *J. Am. Chem. Soc.* 2021, *143*, 20002–20014.

[5] a) A. C. Ghosh, C. Duboc, M. Gennari, *Coord. Chem. Rev.* **2021**, *428*, 213606; b) Y. Maurya, A. Singh, V. Kumar, M. Ul Nisa, S. Chatterjee, *Tetrahedron Lett.* **2024**, *142*, 155066.

[6] a) M. Navarro, J. J. Moreno, M. Pérez-Jiménez, J. Campos, *Chem. Commun.* **2022**, *58*, 11220–11235; b) S. Das, R. Laplaza, J. T. Blaskovits, C. Corminboeuf, *J. Am. Chem. Soc.* **2024**, *146*, 15806–15814.

[7] Q. Wan, S. Lin, H. Guo, *Molecules* **2022**, *27*, 3734.

[8] R. Wischert, P. Laurent, C. Copéret, F. Delbecq, P. Sautet, *J. Am. Chem. Soc.* **2012**, *134*, 14430–14449.

[9] S. Liu, M. Dong, Y. Wu, S. Luan, Y. Xin, J. Du, S. Li, H. Liu, B. Han, *Nat. Commun.* **2022**, *13*, 1–10.

[10] K. K. Ghuman, T. E. Wood, L. B. Hoch, C. A. Mims, G. A. Ozin, C. V. Singh, *Phys. Chem. Chem. Phys.* **2015**, *17*, 14623–14635.

[11] a) S. Zhang, Z. Huang, Y. Ma, W. Gao, J. Li, F. Cao, L. Li, C. Chang, Y. Qu, *Nat. Commun.* **2017**, *8*, 1–11; b) D. Salusso, G. Grillo, M. Manzoli, M. Signorile, S. Zafeiratos, M. Barreau, A. Damin, V. Crocellà, G. Cravotto, S. Bordiga, *ACS Appl. Mater. Interfaces* **2023**, *15*, 15396–15408.

[12] H. Chen, C. Xiong, J. Moon, A. S. Ivanov, W. Lin, T. Wang, J. Fu, D. E. Jiang, Z. Wu, Z. Yang, S. Dai, *J. Am. Chem. Soc.* **2022**, *144*, 10688–10693.

[13] a) E. A. Romero, T. Zhao, R. Nakano, X. Hu, Y. Wu, R. Jazzar, G. Bertrand, *Nat. Catal.* **2018**, *1*, 743–747; b) K. Mentoor, L. Twigge, J. W. H. Niemantsverdriet, J. C. Swarts, E. Erasmus, *Inorg. Chem.* **2021**, *60*, 55–69.

[14] a) P. Colombo, G. Mera, R. Riedel, G. D. Sorarù, *J. Am. Ceram. Soc.* **2010**, *93*, 1805–1837; b) Y. Iwamoto, G. Motz, E. Ionescu, S. Bernard, in *Encycl. Mater. Tech. Ceram. Glas.*, Elsevier, **2021**, pp. 93–102.

[15] M. Alonso, M. C. Garcia, C. McKay, L. R. Thorp, M. Webb, L. J. Edwards, *Org. Process Res. Dev.* **2021**, *25*, 988–1000.

[16] a) V. L. Nguyen, E. Zera, A. Perolo, R. Campostrini, W. Li, G. Domenico, *J. Eur. Ceram. Soc.* **2015**, *35*, 3295–3302; b) Viard, D. Fonblanc, M. Schmidt, A. Lale, C. Salameh, A. Soleilhavoup, M. Wynn, P. Champagne, S. Cerneaux, F. Babonneau, G. Chollon, F. Rossignol, C. Gervais, S. Bernard, *Chem. - A Eur. J.* **2017**, *23*, 9076–9090 ; c) M. Wynn, D. Lopez-Ferber, A. Viard, D. Fonblanc, M. Schmidt, F. Rossignol, P. Carles, G. Chollon, C. Gervais, S. Bernard, *Open Ceramics*, **2021**, *5*, 100055-100067.

[17] a) S. Xie, Y. Song, Z. Liu, *Can. J. Chem.* **2009**, *87*, 1235–1247; b) S. Frueh, R. Kellett, C. Mallery, T. Molter, W. S. Willis, C. King'Ondu, S. L. Suib, *Inorg. Chem.* **2011**, *50*, 783–792.

[18] S. K. Lee, J. F. Stebbins, *Geochim. Cosmochim. Acta* **2003**, *67*, 1699–1709.

[19] a) Z. Hong, D. Y. Ong, S. K. Muduli, P. C. Too, G. H. Chan, Y. L. Tnay, S. Chiba, Y. Nishiyama, H. Hirao, H. Sen Soo, *Chem. - A Eur. J.* **2016**, *22*, 7108–7114; b) I. Hlova, J. F. Goldston, S. Gupta, T. Kobayashi, M. Pruski, V. K. Pecharsky, *J. Mater. Sci.* **2017**, *52*, 11900–11910.

[20] S. Anga, Y. Sarazin, J. F. Carpentier, T. K. Panda, *ChemCatChem* **2016**, *8*, 1373–1378.

[21] D. Fonblanc, D. Lopez-Ferber, M. Wynn, A. Lale, A. Soleilhavoup, A. Leriche, Y. Iwamoto, F. Rossignol, C. Gervais, S. Bernard, *Dalt. Trans.* **2018**, *47*, 14580–14593.

[22] A. O. Maselugbo, J. E. Knoop, K. S. Nowlin, G. Pathiraja, H. B. Harrison, J. R. Alston, *J. Mater. Res.* **2022**, *37*, 4496–4507.

[23] D. Seyferth, G. H. Wiseman, *J. Am. Ceram. Soc.* **1984**, **67**, C-132–C-133.

[24] C. Gervais, F. Babonneau, *J. Organomet. Chem.* **2002**, *657*, 75–82.

[25] G. Jeschke, W. Hoffbauer, M. Jansen, *Solid State Nucl. Magn. Reson.* **1998**, *12*, 1–7.

[26] K. Sardar, R. Bounds, M. Carravetta, G. Cutts, J. S. J. Hargreaves, A. L. Hector, J. A. Hriljac, W. Levason, F. Wilson, *Dalt. Trans.* **2016**, *45*, 5765–5774.

[27] A. Krishnamurthy, V. K. Michaelis, S. Kroeker, *J. Phys. Chem. C* **2021**, *125*, 8815–8824.

[28] a) X. Y. Sun, B. Li, T. F. Liu, J. Song, D. S. Su, *Phys. Chem. Chem. Phys.* **2016**, *18*, 11120–11124; b) X. Liu, X. Wang, Y. Li, T. Yu, W. Zhao, L. Liu, *Phys. Chem. Chem. Phys.* **2021**, *23*, 12541–12548.

[29] C. Schitco, M. S. Bazarjani, R. Riedel, A. Gurlo, *J. Mater. Chem. A* **2015**, *3*, 805–818.

[30] M. Thommes, K. Kaneko, A. V. Neimark, J. P. Olivier, F. Rodriguez-Reinoso, J. Rouquerol, K. S. W. Sing, *Pure Appl. Chem.* **2015**, *87*, 1051–1069.

[31] S. Tada, S. Takazawa, N. Asakuma, M. Cheype, S. Honda, R. Kumar, S. Bernard, Y. Iwamoto, *J. Mater. Chem. A* **2024**, *12*, 3689–3699.

[32] S. Tada, N. Asakuma, S. Ando, T. Asaka, Y. Daiko, S. Honda, M. Haneda, S. Bernard, R. Riedel, Y. Iwamoto, *J. Mater. Chem. A* **2021**, *9*, 2959–2969.

[33] M. Niwa, K. Suzuki, N. Katada, T. Kanougi, T. Atoguchi, *J. Phys. Chem. B* **2005**, *109*, 18749–18757.

[34] K. Pokrovski, K. T. Jung, A. T. Bell, *Langmuir* **2001**, *17*, 4297–4303.

[35] a) M. Faizan, R. Pawar, *J. Phys. Chem. A* **2022**, *126*, 8633–8644; b) R. Pal, M. Ghara, P. K. Chattaraj, *Catalysts* **2022**, *12*, 201.

[36] E. Tal-Gutelmacher, D. Eliezer, E. Abramov, *Mater. Sci. Eng. A* **2007**, *445–446*, 625–631.

[37] J. Zhang, Y. Shao, Y. Li, Y. Liu, Z. Ke, *Chinese Chem. Lett.* **2018**, *29*, 1226–1232.

[38] a) S. C. Kohn, M. E. Smith, P. J. Dirken, E. R. H. Van Eck, A. P. M. Kentgens, R. Dupree, *Geochim. Cosmochim. Acta* **1998**, *62*, 79–87; b) X. Xue, M. Kanzaki, *J. Am. Ceram. Soc.* **2009**, *92*, 2803–2830

[39] S. Widgeon, G. Mera, Y. Gao, E. Stoyanov, S. Sen, A. Navrotsky, R. Riedel, *Chem. Mater.* **2012**, *24*, 1181–1191.

[40] J. Zhang, S. Hu, Y. Wang, *RSC Adv.* **2014**, *4*, 62912–62919.

[41] a) B. L. J. Poad, P. J. Wearne, E. J. Bieske, A. A. Buchachenko, D. I. G. Bennett, J. Kłos, M. H. Alexander, *J. Chem. Phys.* **2008**, *18*, 129; b) V. Dryza, E. J. Bieske, *Int. Rev. Phys. Chem.* **2013**, 32, 559–587;

[42] a) T. Gullion and J. Schaefer, *J. Magn. Reson.*, **1989**, *81*, 196–200; b) M. Bertmer, H. Eckert, *Solid State Nucl. Magn. Reson.* **1999**, *15*, 139–152; c) T. Gullion, *Mod. Magn. Reson.* **2007**, *1*, 713–718.

[43] S. Pattisson, E. Nowicka, U. N. Gupta, G. Shaw, R. L. Jenkins, D. J. Morgan, D. W. Knight, G. J. Hutchings, *Nat. Commun.* **2016**, *7*, 12855.

[44] a) C. Salameh, A. Bruma, S. Malo, U. B. Demirci, P. Miele, S. Bernard, *RSC Adv.* **2015**, *5*, 58943–58951; b) C. Durif, M. Wynn, M. Balestrat, G. Franchin, Y.-W. Kim, A. Leriche, P. Miele, P. Colombo, S. Bernard, *J. Eur. Ceram. Soc.* **2019**, *39*, 5114–5122.

[45] M. Cheype, V. Pateloup, S. Bernard, *Adv. Mater.* **2024**, *36*, 2307554

[46] R. S. Mikhail, S. Brunauer, E. E. Bodor, *J. Colloid Interface Sci.* **1968**, *26*, 45–53.

[47] E. P. Barrett, L. G. Joyner, P. P. Halenda, *J. Am. Chem. Soc.* **1951**, *73*, 373–380.

Novel Lewis Acid-Base Interactions in Polymer-Derived Sodium-Doped Amorphous Si-B-N Ceramic: Towards Main-Group-Mediated Hydrogen Activation

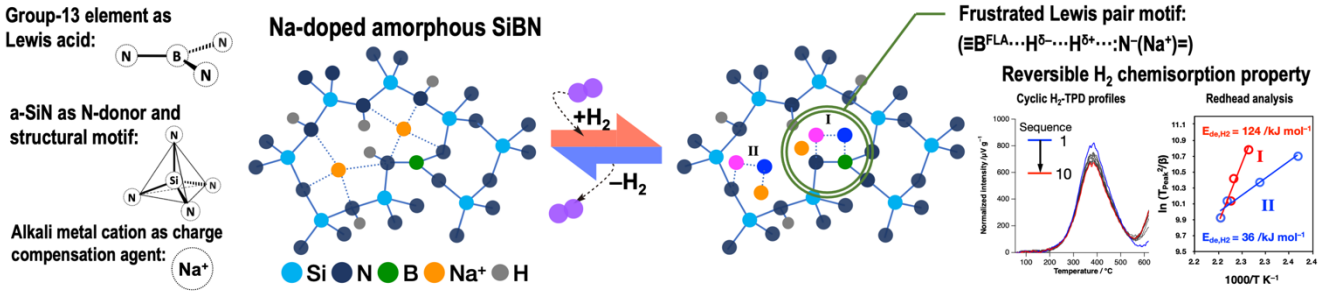

We explored the Polymer-Derived Ceramics route to design and synthesize a transition metal-free sodium-doped amorphous SiBN ceramic, for small molecule activation and catalysis. The distribution of molecular Na^+ and B sites in amorphous silicon nitride amplified B and N site reactivity, forming a frustrated Lewis pair (FLP) motif upon H_2 exposure. This FLP-inspired approach promises advances in main-group-mediated heterogeneous catalysis.